

Mathematical Model and Simulation of Cutting Layer Geometry in Orthogonal Turn-Milling with Zero Eccentricity

SUN Tao¹, QIN Lufang¹, FU Yucan^{2*}, HOU Junming³

1. Jiangsu Key Laboratory of Engineering Machinery Detection and Control, Xuzhou University of Technology, Xuzhou 221111, P. R. China;
2. College of Mechanical and Electrical Engineering, Nanjing University of Aeronautics and Astronautics, Nanjing 210016, P. R. China;
3. Industrial Center, Nanjing Institute of Technology, Nanjing 211167, P. R. China

(Received 2 March 2020; revised 20 April 2020; accepted 5 June 2020)

Abstract: Orthogonal turn-milling is a high-efficiency and precision machining method. Its cutting layer directly affects chip formation, cutting forces, and chatter, and further affects tool life, machining quality, etc. We studied The cutting layer geometry (CLG) in orthogonal turn-milling with zero eccentricity (OTMZE) is studied to explore orthogonal turn-milling cutting layer formation process. OTMZE principles of motion and formation processes are analyzed statically without considering kinetic influences. Mathematical models of the entrance and exit angles, cutting thickness, and cutting depth are established. In addition, these models are validated experimentally and some influences of cutting parameters on the tool cutting layer are analyzed. The results show that OTMZE cutting layer formation can be divided into two stages, chip shapes are nearly consistent with the simulated CLGs, and the most influential parameter in affecting the cutting layer is found to be the tool feed per revolution of workpiece f_a , followed by the ratio of the tool and workpiece speeds λ and the cutting depth a_p . These models and results can provide theoretical guidance to clarify formation processes and quantitatively analyze changes in cutting layer geometry during OTMZE. In addition, they offer theoretical guidelines for cutting forces and chatter.

Key words: orthogonal turn-milling; zero eccentricity; cutting layer geometry; mathematical model; forming process

CLC number: TG506.9 **Document code:** A **Article ID:** 1005-1120(2020)06-0839-09

0 Introduction

Orthogonal turn-milling can achieve high-efficiency and high-precision machining by combining workpiece rotation with rotation and axial movement of a milling cutter along the workpiece. It is widely used to machine difficult-to-cut materials such as Ti alloys, nickel alloys, and stainless steels as well as special structural components (e.g., crankshafts, slender rods, turbine blades, and engine casings)^[1-2].

Chip formation, cutting forces, and chatter are important orthogonal turn-milling research topics that affect machining efficiency, machining quality,

and tool life^[3-5]. Orthogonal turn-milling differs from turning and milling such that the cutting layer geometries (CLGs) of their steps are completely different. Understanding the geometries and mathematical models of orthogonal turn-milling cutting layers is useful when researching chip formation, cutting forces, and chatter.

Zhu et al. established mathematical models of orthogonal turn-milling CLGs based on two conditions of zero eccentricity and eccentricity. The researchers simulated and predicted chip shapes, cutting forces, and chatter^[6-8]. Yan and Sun et al. analyzed orthogonal turn-milling cutting chatter by building mathematical CLG models that considered

*Corresponding author, E-mail address: yucanfu@nuaa.edu.cn.

How to cite this article: SUN Tao, QIN Lufang, FU Yucan, et al. Mathematical model and simulation of cutting layer geometry in orthogonal turn-milling with zero eccentricity[J]. Transactions of Nanjing University of Aeronautics and Astronautics, 2020, 37(6): 839-847.

<http://dx.doi.org/10.16356/j.1005-1120.2020.06.002>

eccentricity^[9-10]. Karagüzel, Kara, and Crichigno et al. established a mathematical CLG model with zero eccentricity and a simulated orthogonal turn-milling cutting force^[11-14]. Yan et al. created a mathematical CLG model with zero eccentricity using a helical milling cutter and predicted the corresponding cutting force^[15].

Although there are reports on orthogonal turn-milling CLGs, several problems remain to be solved: (i) detailed analyses of cutting layer formation are lacking; (ii) the mathematical CLG models built thus far are complex; (iii) the validated CLG methods are relatively simple; (iv) there is a lack of analysis of the influences of cutting parameters on CLGs.

CLGs from orthogonal turn-milling with zero eccentricity (OTMZE) are more complex than those applicable to orthogonal turn-milling with eccentricity. Thus, we research OTMZE CLG mathematical modeling and simulation. This work investigates the principles of motion behind OTMZE. We analyze the CLG formation process and establish CLG mathematical models. In addition, we perform experiments to confirm mathematical model accuracy by comparing the shapes, volumes, and maximum cutting depths of various simulated CLGs to those from actual chips. Finally, we simulate and analyze the influences of cutting parameters on CLGs. Thus, the aim of this paper is to provide a theoretical guide to the cutting force and chatter in orthogonal turn-milling.

1 Cutting Layer Formation During OTMZE

1.1 Cutting layer motion principle

In orthogonal turn-milling, we assume that the workpiece is at rest and the tool moves spirally along the axis of the workpiece (x_w). The three axes x_w , y_w , and z_w are shown in Fig.1, where r_w is the workpiece radius, r_t the tool radius, n_w the workpiece speed, n_t the tool speed, and a_p the cutting depth. The intersected portion of the two tool positions and the workpiece produced when the tool moves from position 1 to position 2 can be viewed

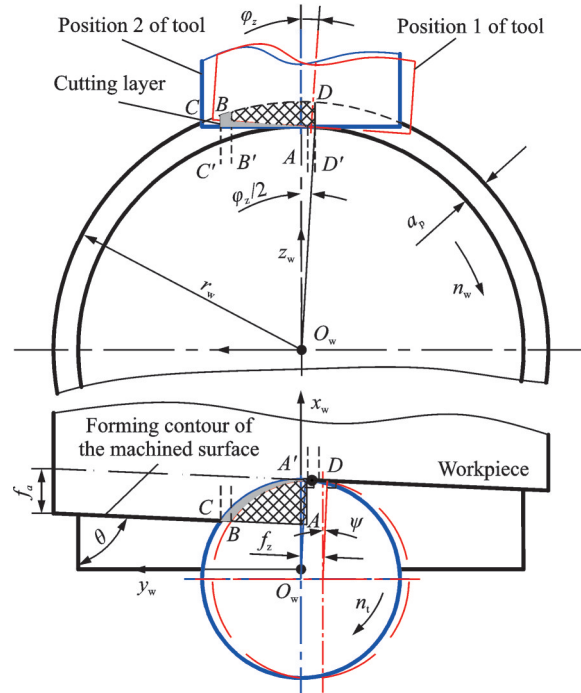


Fig.1 Principle diagram of motion during OTMZE

as the OTMZE CLG. Thus, the layer cutting process is analyzed statically without considering kinetic influences.

During the OTMZE cutting process, the side cutting edges corresponding to two separate tool positions cut the forming contour of the machined workpiece surface at two lines BB' and CC' that meet at line DD' . The edges respectively cut the workpiece at two arcs CD and BD and the area from arc CD turning right into arc BD is formed by side cutting edge. The bottom cutting edges corresponding to the two tool positions meet at line AA' . Line AA' is at the right of arc BD . The area from arc BD turning right into line AA' is formed by the bottom cutting edge. The above analyses indicate that the side and bottom cutting edges participate in simultaneous cutting. Thus, the entrance and exit angles of the side and bottom cutting edges must be considered during analysis of OTMZE.

In the cutting process of OTMZE, the corresponding rotation angle of the workpiece is φ_z while a milling cutter blade is rotated as shown in Fig.1. The angle φ_z can be expressed as

$$\varphi_z = \frac{2\pi}{\lambda Z} \quad (1)$$

where λ is the ratio of the tool and workpiece speeds

(i.e., $\lambda = n_t/n_w$) and Z the number of teeth on the tool.

In Fig.1, θ is the forming contour angle of the machined workpiece surface.

$$\theta = \arctan [2\pi \cdot (r_w - a_p) / f_a] \quad (2)$$

where f_a is the tool feed per revolution of workpiece.

The line through the center point of the tool position is perpendicular to the workpiece forming contour. In this analysis, ψ is the angle between the perpendicular line and the center line of the tool position (direction of x_w) and f_z is the distance that the tool moves along the forming contour of the workpiece when the workpiece is rotated the angle (φ_z). They can be expressed as

$$\psi = \frac{\pi}{2} - \theta \quad (3)$$

$$f_z = \frac{\sqrt{f_a^2 + [2\pi(r_w - a_p)]^2}}{Z \cdot \lambda} \quad (4)$$

1.2 Cutting layer formation process

The fillet radius of the tool used in orthogonal turn-milling is usually less than 0.8 mm. Thus, the influence of the tool fillet radius on the cutting layer geometry is negligible and can be ignored. To simplify the calculation, the fillet radius of the tool is not considered in our analyses.

The cutting layer formation process involves parameters such as the entrance and exit angles, cutting depth, and cutting thickness, as shown in Fig.2. During OTMZE cutting, the side cutting edge cuts into the workpiece from point C first. Next, the side and bottom cutting edges cut into the workpiece from point B simultaneously. Then, the bottom cutting edge cuts the workpiece from points A and A' , and finally the side cutting edge cuts out the workpiece from point D . The entrance and exit angles corresponding to the above process are respectively $\varphi_{st,C}$, $\varphi_{st,B}$, $\varphi_{ex,A}$, $\varphi_{ex,A'}$, and $\varphi_{ex,D}$.

In Fig.2, φ_i is the dynamic contact angle of tooth i as it cuts the workpiece. The cutting thickness and depth of the side cutting edge of tooth i at φ_i are $h_p(\varphi_i)$ and $a_p(\varphi_i)$, respectively. While $h_t(\varphi_i)$ and $a_t(\varphi_i)$ are the cutting thickness and depth of the bottom cutting edge of tooth i at φ_i , respectively.

The various OTMZE tool entrance and exit an-

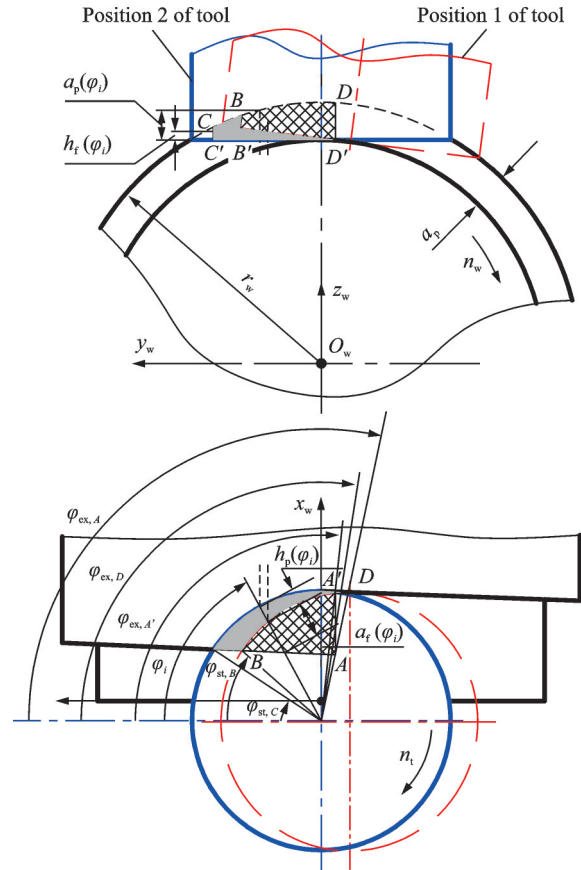


Fig.2 OTMZE cutting parameters

gles allow one to divide the cutting layer into four stages: $\varphi_{st,C} \leq \varphi_i \leq \varphi_{st,B}$, $\varphi_{st,B} < \varphi_i \leq \varphi_{ex,A'}$, $\varphi_{ex,A'} < \varphi_i \leq \varphi_{ex,D}$, and $\varphi_{ex,D} < \varphi_i \leq \varphi_{ex,A}$. The differences between the angles $\varphi_{ex,A'}$, $\varphi_{ex,D}$, and $\varphi_{ex,A}$ are negligible during cutting, so they can be replaced by a single angle $\varphi_{ex,D}$. Finally, the cutting layer can be simplified to two stages of $\varphi_{st,C} \leq \varphi_i \leq \varphi_{st,B}$ and $\varphi_{st,B} < \varphi_i \leq \varphi_{ex,D}$, as shown in Fig.3.

During the $\varphi_{st,C} \leq \varphi_i \leq \varphi_{st,B}$ stage, the side cutting edge forms the cutting layer shown in Fig.3. The left side of the cutting layer cross-section is a plumb line that represents the intersection of the side cutting edge from position 2 of tool and the cut-away plane $a-a$. To the right is another plumb line

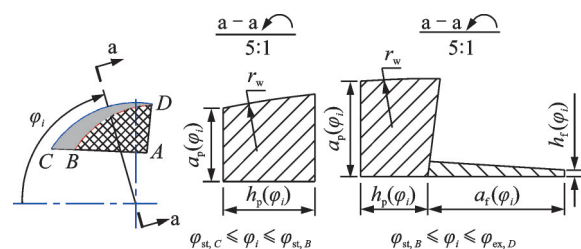


Fig.3 OTMZE cutting layer cross-sections

that represents the intersection of the workpiece forming the contour and the cutaway plane a-a. The bottom is a horizontal line that represents the intersection of the plane a-a and the bottom cutting edge from position 2 of the tool. The top is an arc that represents the intersection of the cylindrical workpiece surface and the plane a-a. The arc is short enough that it can be considered equivalent to a straight line.

In the $\varphi_{st,B} \leq \varphi_i \leq \varphi_{ex,D}$ stage, the side and bottom edges cut simultaneously. Together, they form the cutting layer shown in Fig. 3. The cutting layer consists of two parts: the part formed by the side cutting edge on the left and the part formed by the bottom cutting edge on the right.

To the left of the cross-section of the cutting layer formed by the side cutting edge is a plumb line that represents the intersection of the side cutting edge from position 2 of the tool and the cutaway plane a-a. To the right of that is a line that represents the intersection of the side cutting edge from position 1 of the tool and the plane a-a. This is an oblique line with a small φ_z that can be treated as a plumb line. The bottom is a horizontal line that represents the intersection of the bottom cutting edge from position 2 of the tool and the plane a-a. The top is an arc that can be treated as a straight line, as in the above analysis of the $\varphi_{st,C} \leq \varphi_i \leq \varphi_{st,B}$ stage.

To the left of the cross-section of the cutting layer formed by the bottom cutting edge is a line that represents the intersection of the envelope region produced when moving from position 1 to point 2 of the tool and the cutaway plane a-a. This line is common with the right side of the cutting layer produced by the side cutting edge. To the far right is a plumb line that represents the intersection of the workpiece forming contour and the plane a-a. The bottom is a horizontal line that represents the intersection of the bottom cutting edge from position 2 of the tool and the plane a-a. This line is common with that from the bottom of the cutting layer produced by the side cutting edge. The top is a line that represents the intersection of the bottom cutting edge from position 1 of the tool and the plane a-a. This is an oblique line with a negligibly small φ_z such that it

can be treated as a horizontal line. That is, the top of the cross-section of the cutting layer formed by the bottom cutting edge can be regarded as parallel to the bottom of the layer.

2 Mathematical Model of OTMZE CLG

The above analyses indicate that the cutting layer angle ranges formed by the side and bottom cutting edges are $\varphi_{st,C} \leq \varphi_i \leq \varphi_{ex,D}$ and $\varphi_{st,B} \leq \varphi_i \leq \varphi_{ex,D}$, respectively. The mathematical models of tool entrance and exit angles during OTMZE can be expressed as

$$\begin{cases} \varphi_{st,C} = \arcsin(1 - f_a \cdot \cos\psi / r_t) + \psi \\ \varphi_{st,B} = \arctan\left(\frac{r_t - f_a \cdot \cos\psi}{\sqrt{2r_t \cdot f_a \cdot \cos\psi - f_a^2 \cdot \cos^2\psi - f_z}}\right) + \psi \\ \varphi_{ex,D} = \arctan(0.5f_z / r_t) + \psi + \pi/2 \end{cases} \quad (5)$$

The cutting thicknesses of the cutting layers formed by the side and bottom cutting edges [$h_p(\varphi_i)$ and $h_t(\varphi_i)$] are

$$\begin{cases} h_p(\varphi_i) = r_t - y_1 & \varphi_{st,C} \leq \varphi_i \leq \varphi_{st,B} \\ h_p(\varphi_i) = f_z \cdot \cos(\varphi_i - \psi) + r_t - y_2 & \varphi_{st,B} < \varphi_i \leq \varphi_{ex,D} \\ h_t(\varphi_i) = (y_1 \cdot \cos\varphi_i + y_3) \cdot \tan\varphi_z & \varphi_{st,B} < \varphi_i \leq \varphi_{ex,D} \end{cases} \quad (6)$$

where y_1 , y_2 , and y_3 are variables that are defined as follows: $y_1 = (r_t - f_a \cdot \cos\psi) / \sin(\varphi_i - \psi)$, $y_2 = [r_t^2 - (f_z \cdot \sin(\varphi_i - \psi))^2]^{1/2}$, and $y_3 = (r_w - a_p) \cdot \tan(0.5\varphi_z)$.

The cutting depths of the cutting layers formed by the side and bottom cutting edges $a_p(\varphi_i)$ and $a_t(\varphi_i)$ are

$$\begin{cases} a_p(\varphi_i) = \sqrt{r_w^2 - (r_t \cdot \cos\varphi_i)^2} - r_w + a_p & \varphi_{st,C} \leq \varphi_i \leq \varphi_{ex,D} \\ a_t(\varphi_i) = y_2 - f_z \cdot \cos(\varphi_i - \psi) - y_1 & \varphi_{st,B} \leq \varphi_i \leq \varphi_{ex,D} \end{cases} \quad (7)$$

3 Experimental Tests

The machine tool used for experiments is a Mazak Integrex 200-IVST. The experimental cutting tool includes a toolholder and an insert, as shown in Fig. 4. The specification of the insert is ISO standard R390-11 T3 08E-PLW 1130 (Sandvik), and the rake and clearance angles are 16° and

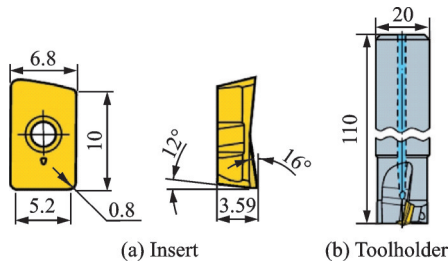


Fig.4 Dimensions of the insert and tool holder used in turn-milling

12°, respectively. The specification of the tool holder is ISO standard R390-020A22-11M and the cutting diameter is 20 mm.

The OTMZE cutting parameters are as follows: $r_w=40$ mm, $r_t=10$ mm, $a_p=1$ mm, $f_a=3$ mm/r, $Z=1$, and $\lambda=50$. CLGs and tool relationships simulated using the OTMZE CLG mathematical model described in Eqs. (5)–(7) via software UG and Matlab are shown in Fig. 5(a). Actual OTMZE chips are measured using a digital measuring microscope (ISM-DL301-Y), as shown in Figs. 5(b) and 5(c).

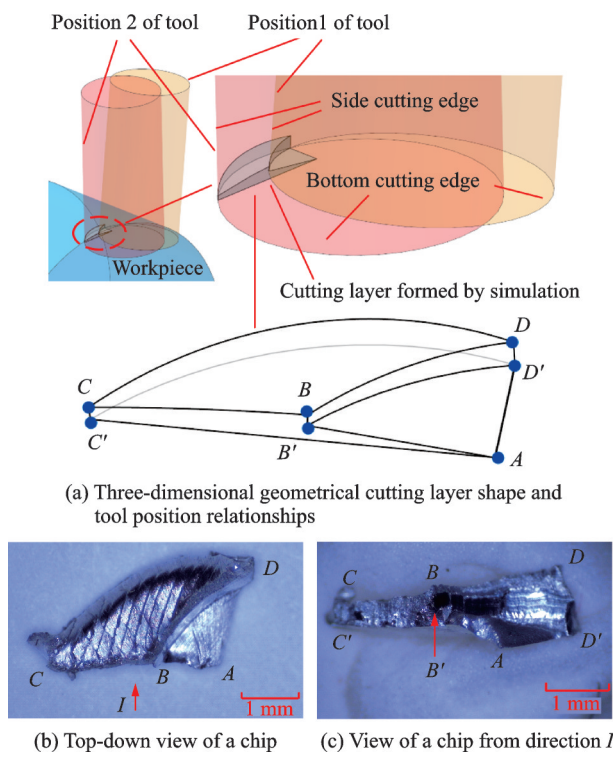


Fig.5 OTMZE CLG experimental test

Although the chip is substantially deformed, its shape appears generally consistent with the simulated CLG upon analysis. As the tool moves from

position 1 to position 2, the contours of the cutting layer formed by the side cutting edges are the surfaces $BB'D'D$ and $CC'D'D$. The bottom cutting edges formed the surfaces $B'AD'$ and $C'AD'$. The lines BB' , CC' , DD' , and AD' coincided with the simulated CLG. The results confirm that the CLG mathematical models in this paper are correct.

The cutting depth and cutting layer volume are two important cutting parameters reflecting the CLG. The cutting depth used in turning and milling is constant, while that of turn-milling changes. Thus, the maximum cutting depth a_{pmax} (the vertical distance from point B to the surface $C'AD'$ in Fig.5) can be compared to the simulated CLG and chip measurements shown in Fig.6(a). The chip volume can not be measured directly. Instead, an electronic scale with a precision of 0.01 g is used to measure the chip weight and the chip volume is calculated indirectly using the material density of the workpiece. The chip volume from the simulated CLG is contrasted with the measured quantity in Fig.6(b).

In the theoretical case, the maximum cutting depth a_{pmax} does not exceed the cutting depth a_p . In Fig.6(a), the a_{pmax} measured on a chip exceeds the

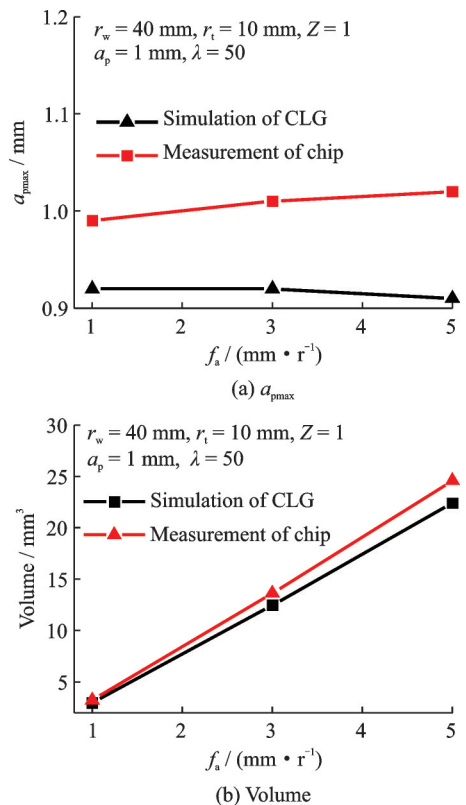


Fig.6 OTMZE chip simulation and experimental results

a_p ($a_p=1$ mm) caused by machining deformation. The a_{pmax} values from the CLG simulation are 0.92 mm, 0.92 mm, and 0.91 mm, while the a_{pmax} values measured from chips are 0.99 mm, 1.01 mm, and 1.02 mm when $f_a = 1$ mm/r, 3 mm/r, and 5 mm/r, respectively. The forecasting errors are 7.61%, 9.78%, and 12.09%, respectively.

In Fig. 6(b), the simulated chip volumes are 2.95 mm³, 12.47 mm³, and 22.39 mm³ while the measured volumes are 3.21 mm³, 13.63 mm³, and 24.58 mm³ when $f_a = 1$ mm/r, 3 mm/r, and 5 mm/r, respectively. The forecasting errors are 8.81%, 9.3%, and 9.78%, respectively.

The above comparisons and analyses of results show that the simulated and measured values are quite similar. In addition, the simulated CLG coincides with the geometry of actual chip. This demonstrates that the mathematical modeling of CLG performed in Section 2 is accurate and feasible.

4 OTMZE Cutting Layer Analyses

The side and bottom cutting edges participate simultaneously in cutting and form cutting layers during OTMZE. To analyze OTMZE cutting layer changes further, data is generated using Eqs. (5)–(7) and cutting thicknesses and cutting layer depths are determined and analyzed using the data.

4.1 Effect of parameters on cutting layer formed by the side cutting edge

The cutting thicknesses and depths formed by a side cutting edge with φ_i are $h_p(\varphi_i)$ and $a_p(\varphi_i)$, respectively, as shown in Fig. 7. As φ_i increases, $h_p(\varphi_i)$ increases from zero to its maximum and then decreases from its maximum to zero, while $a_p(\varphi_i)$ increases to its maximum.

As shown in Fig. 7(a), given that $a_p = 1.5$ mm, and $\lambda=80$, $\varphi_{st,C1}$, $\varphi_{st,C2}$, and $\varphi_{st,C3}$ are the dynamic contact angles of tooth i at point C of the cutting workpiece (i.e. the entrance angle of the side cutting edge) when $f_a = 3$ mm/r, 5 mm/r, and 7 mm/r, respectively. The entrance angle of the side cutting edge at point C $\varphi_{st,C}$ decreases as f_a increases.

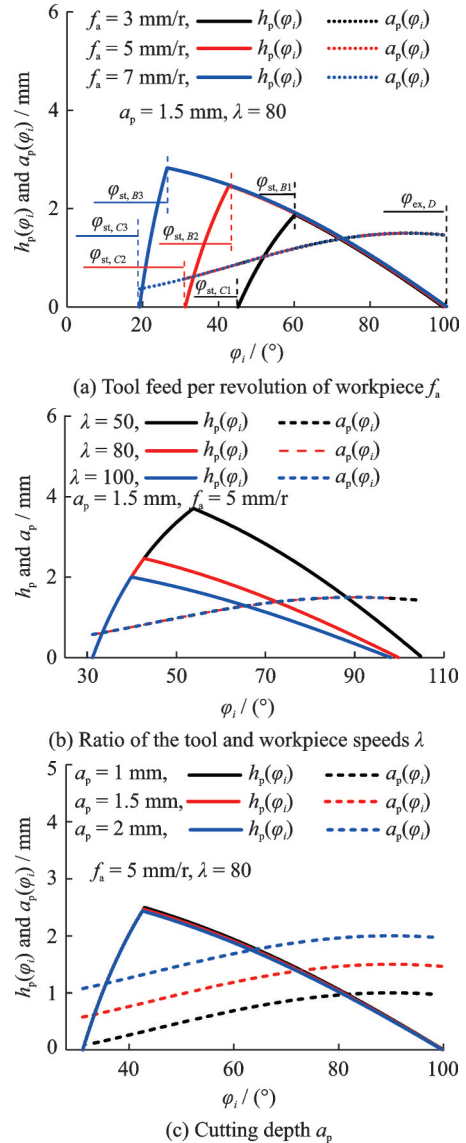


Fig. 7 Effect of parameters on cutting layer formed by side cutting edge ($r_w=40$ mm, $r_t=10$ mm, $Z=1$)

Here, $\varphi_{st,B1}$, $\varphi_{st,B2}$, and $\varphi_{st,B3}$ are the dynamic contact angles of tooth i at point B of the cutting workpiece when $f_a = 3$ mm/r, 5 mm/r, and 7 mm/r, respectively. The entrance angle of the side cutting edge at point B $\varphi_{st,B}$ is also the entrance angle of the bottom cutting edge. We note that $\varphi_{st,B}$ decreases as f_a increases.

Here, $\varphi_{ex,D}$ is the dynamic contact angle of tooth i at point D of the cutting workpiece (i.e. the exit angle of the side and bottom cutting edges). The change in φ_D as f_a increases is quite small. We note that $\varphi_{st,C}$ and $\varphi_{st,B}$ decrease and $\varphi_{ex,D}$ is nearly unchanged as f_a increases, so the range of the cutting layer grows.

It can be seen from Fig.7(a) that the maximum of $h_p(\varphi_i)$ increases but the maximum of $a_p(\varphi_i)$ is unchanged as f_a increases. Moreover, the rising trend of $h_p(\varphi_i)$ from zero to its maximum becomes steeper, while the descending trend of $h_p(\varphi_i)$ from its maximum to zero and the rising trend of $a_p(\varphi_i)$ are unchanged as f_a increases. The steeper $h_p(\varphi_i)$ curve indicates that the cutting layer formed only by the side cutting edge (i.e. the cutting layer from point C to point B) shrinks.

As shown in Fig.7(b), $\varphi_{st,C}$ is unchanged and $\varphi_{st,B}$ and $\varphi_{ex,D}$ decrease as λ increases when $a_p=1.5$ mm, and $f_a=5$ mm/r. This shows that both the cutting layer formed by only the side cutting edge and its range decrease. The maximum of $h_p(\varphi_i)$ decreases and the maximum of $a_p(\varphi_i)$ is unchanged as λ increases. Moreover, the rising trends of $h_p(\varphi_i)$ and $a_p(\varphi_i)$ are unchanged and the decreasing trend of $h_p(\varphi_i)$ becomes flatter as λ increases.

As shown in Fig.7(c), when $f_a=5$ mm/r, and $\lambda=80$, $\varphi_{st,C}$ is unchanged and the changes in $\varphi_{st,B}$ and $\varphi_{ex,D}$ with increasing a_p are quite small. This shows that both the cutting layer formed only by the side cutting edge and its range are nearly unchanged. The maximum, rising trend, and decreasing trend of $h_p(\varphi_i)$ are nearly unchanged. Moreover, $a_p(\varphi_i)$ increases with a_p and the rising trend of $a_p(\varphi_i)$ changes little.

4.2 Effects of parameters on cutting layer formed by bottom cutting edge

The cutting thicknesses and depths formed by the bottom cutting edge of a tool with φ_i are $h_t(\varphi_i)$ and $a_t(\varphi_i)$, respectively, as shown in Fig.8. As φ_i increases, $h_t(\varphi_i)$ decreases from its maximum to zero and $a_t(\varphi_i)$ increases from zero to its maximum.

As shown in Fig.8(a), $\varphi_{st,B}$ decreases and $\varphi_{ex,D}$ is nearly unchanged as f_a increases. Thus, the cutting layer formed by only the bottom cutting edge enlarges. Moreover, the maxima of $h_t(\varphi_i)$ increase slightly and those of $a_t(\varphi_i)$ increase substantially, the decreasing trend of $h_t(\varphi_i)$ shrinks, and the rising trend of $a_t(\varphi_i)$ is nearly unchanged.

As shown in Fig.8(b), $\varphi_{st,B}$ and $\varphi_{ex,D}$ both decrease as λ increases when $a_p=1.5$ mm, and $f_a=$

5 mm/r. This shows that the cutting layer formed by only the bottom cutting edge may not change. Moreover, the maxima of $h_t(\varphi_i)$ and $a_t(\varphi_i)$ decrease as λ increases. In addition, the decreasing trend of $h_t(\varphi_i)$ shrinks and the rising trend of $a_t(\varphi_i)$ begins to change.

As shown in Fig.8(c), $\varphi_{st,B}$ and $\varphi_{ex,D}$ remain constant as a_p increases when $f_a=5$ mm/r, and $\lambda=80$. This shows that the cutting layer formed by only the bottom cutting edge remains unchanged. Moreover, the curves of $h_t(\varphi_i)$ and $a_t(\varphi_i)$ remain unchanged. This indicates that a_p has no influence on the cutting layer formed by the bottom cutting edge.

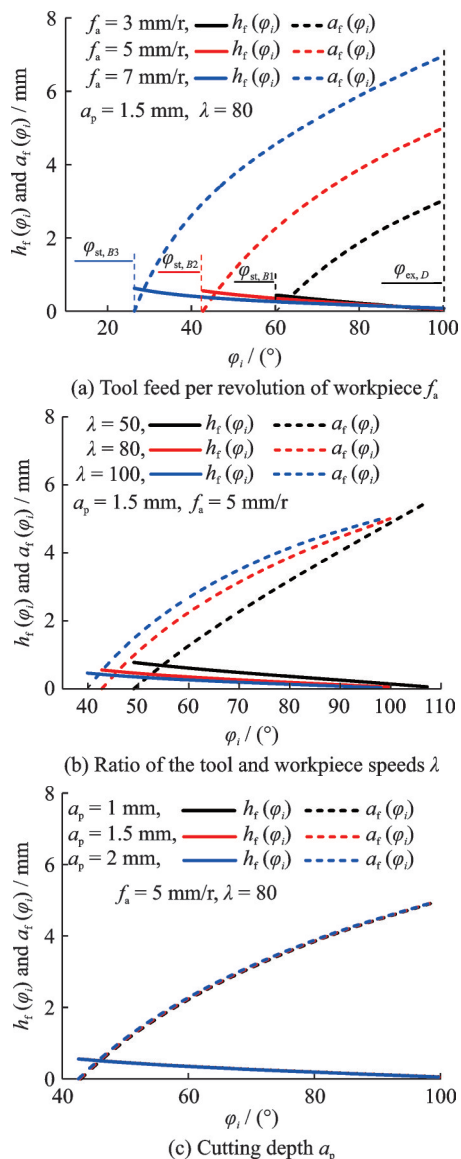


Fig.8 Effects of parameters on cutting layer formed by bottom cutting edge ($r_w=40$ mm, $r_t=10$ mm, $Z=1$)

5 Conclusions

(1) Based on the principles of motion and variation in the OTMZE tool entrance and exit angles, the cutting layer can be divided into two stages: $\varphi_{st,C} \leq \varphi_i \leq \varphi_{st,B}$ and $\varphi_{st,B} < \varphi_i \leq \varphi_{ex,D}$. The cutting layer is formed by the side cutting edge in the former stage and by both the side and bottom cutting edges in the latter stage. The prerequisites of the OTMZE CLG mathematical models are as follows: The entrance and exit angles of the side and bottom cutting edges ($\varphi_{st,C}$, $\varphi_{st,B}$, and $\varphi_{ex,D}$); the cutting thicknesses of the cutting layers formed by the side and bottom cutting edges [$h_p(\varphi_i)$ and $h_t(\varphi_i)$]; and the cutting depths of the cutting layers formed by the side and bottom cutting edges [$a_p(\varphi_i)$ and $a_t(\varphi_i)$].

(2) The three-dimensional geometrical cutting layer shape is simulated using the above mathematical model. Tool position relationships during formation of the shape are discussed to validate the accuracies of the forming process analysis and CLG mathematical models in OTMZE. Moreover, the following experimental chip and simulated CLG data are compared to validate mathematical model accuracy: (i) Shape and profile, (ii) maximum cutting depth a_{pmax} , and (iii) volume. Contrasting experimental and analytical results show that the chip shapes are mostly consistent with the simulated CLGs. The errors in the simulated a_{pmax} and volume do not exceed 12.09% and 9.78%, respectively.

(3) As φ_i increases, $h_p(\varphi_i)$ increases from zero to its maximum and then decreases back to zero, $a_p(\varphi_i)$ increases to its maximum, $h_t(\varphi_i)$ decreases from its maximum to zero and $a_t(\varphi_i)$ increases from zero to its maximum. As f_a increases, the cutting layer range becomes larger, while the cutting layers formed by the side and bottom cutting edges become smaller and larger, respectively. The maximum of $h_p(\varphi_i)$ increases while that of $a_p(\varphi_i)$ remains unchanged, the maximum of $h_t(\varphi_i)$ increases slightly, and that of $a_t(\varphi_i)$ increases substantially. When λ increases, the range of the cutting layer shrinks. In addition, the cutting layer formed by only the side cutting edge shrinks while that formed by the bottom cutting edge does not change. In addition,

the maxima of $h_p(\varphi_i)$, $h_t(\varphi_i)$, and $a_t(\varphi_i)$ decrease while that of $a_p(\varphi_i)$ is unchanged. As a_p increases, the cutting layer range and the cutting layers formed by only the side and bottom cutting edges, respectively, are nearly unchanged. In addition, $h_p(\varphi_i)$ is nearly unchanged, $a_p(\varphi_i)$ increases, and $h_t(\varphi_i)$ and $a_p(\varphi_i)$ are unchanged.

References

- [1] SUN Tao, FU Yucan, HE Lei, et al. Application and development of turn-milling technology for aeronautic components[J]. *Aeronautical Manufacturing Technology*, 2016(6): 16-24. (in Chinese)
- [2] SUN T, FU Y C, HE L, et al. Machinability of plunge milling for damage-tolerant titanium alloy TC21[J]. *The International Journal of Advanced Manufacturing Technology*, 2016, 85 (5/6/7/8): 1315-1323.
- [3] XAVIER B, ASIER B, KAAAN E, et al. Limiting factors for active suppression of structural chatter vibrations using machine's drives[J]. *Transactions of Nanjing University of Aeronautics and Astronautics*, 2017, 34(4): 341-348.
- [4] HUAN H X, XU J H, SU H H, et al. Milling machinability of TiC particle and TiB whisker hybrid reinforced titanium matrix composites[J]. *Transactions of Nanjing University of Aeronautics and Astronautics*, 2017, 34(4): 363-371.
- [5] WAN Min, LI Shaoen, YUAN Heng, et al. Cutting force modeling in milling of CFRP[J]. *Journal of Nanjing University of Aeronautics & Astronautics*, 2019, 51(3): 272-280. (in Chinese)
- [6] ZHU L D, LI H, LIU C. Analytical modeling on 3D chip formation of rotary surface in orthogonal turn-milling[J]. *Archives of Civil and Mechanical Engineering*, 2016, 16(4): 590-604.
- [7] ZHU Lida, LI Hu, YANG Jianyu, et al. Research on theoretical modeling of 3D chip of orthogonal turn-milling[J]. *Journal of Northeastern University (Natural Science)*, 2012, 33(1): 111-115. (in Chinese)
- [8] ZHU Lida, WANG Wanshan, LI Hu, et al. Research on 3D chatter stability of orthogonal and eccentric turn-milling[J]. *Journal of Mechanical Engineering*, 2011, 47(23): 186-192. (in Chinese)
- [9] YAN R, TANG X, PENG F Y, et al. The effect of variable cutting depth and thickness on milling stability for orthogonal turn-milling[J]. *The International Journal of Advanced Manufacturing Technology*, 2016, 82 (1): 765-777.
- [10] SUN T, QIN L F, FU Y C, et al. Chatter stability of orthogonal turn-milling analyzed by complete discreti-

- zation method[J]. Precision Engineering, 2019, 56: 87-95.
- [11] KARAGÜZEL U, UYSAL E, BUDAK E, et al. Analytical modeling of turn-milling process geometry, kinematics and mechanics[J]. International Journal of Machine Tools and Manufacture, 2015, 91: 24-33.
- [12] KARAGÜZEL U, BAKKAL M, BUDAK E. Mechanical and thermal modeling of orthogonal turn-milling operation[J]. Procedia CIRP, 2017, 58: 287-292.
- [13] KARA M E, BUDAK E. Optimization of turn-milling processes[J]. Procedia CIRP, 2015, 33: 477-484.
- [14] CRICHIGNO FILHO J M. Prediction of cutting forces in mill turning through process simulation using a five-axis machining center[J]. The International Journal of Advanced Manufacturing Technology, 2012, 58 (1/2/3/4): 71-80.
- [15] YAN Rong, QIU Feng, PEMG Fangyu, et al. Modeling and analysis of cutting forces in orthogonal turn-milling shaft parts with helical end mills[J]. Journal of Huazhong University of Science and Technology (Natural Science Edition), 2014, 42(5): 1-5.(in Chinese)

Acknowledgements This work was supported by the National Natural Science Foundation of China (No. 51475233), the Natural Science Foundation of Jiangsu Province (No. BK20171170), the Six Talent Peaks Project of Jiangsu Province (No. JXQC-049), the Major Program of the Natural Science Foundation for Colleges and Universities of Jiangsu Province (No. 19KJA560007), and the Project of Jiangsu Key Laboratory of Large Engineering Equipment Detection and Control (No. JSKLEDC201512).

Authors Dr. SUN Tao received his B. S. degree in Me-

chanical Engineering from Tianjin University of Technology and Education in 2003, his M.S. degree in Mechanical Engineering from Lanzhou University of Technology in 2010, and his Ph.D. in Mechanical Engineering from Nanjing University of Aeronautics and Astronautics in 2017. He joined Xuzhou University of Technology in August of 2003, where he is an associate professor at the School of Mechanical and Electrical Engineering. His research is focused on high-efficiency, precision machining and relevant fields.

Prof. FU Yucan received his Ph.D. degree in Mechanical Engineering from Nanjing University of Aeronautics and Astronautics in 1999 after receiving B.S. and M.S. degrees in Mechanical Engineering from Huaqiao University in 1993 and 1996, respectively. He has been with the College of Mechanical and Electrical Engineering, Nanjing University of Aeronautics and Astronautics since 2001. He is currently a full professor and dean of the college. His research is focused on high-efficiency, precision machining, super-hard abrasive tools, green and high-efficiency cooling, and relevant fields.

Author contributions Dr. SUN Tao designed the study, established mathematical modeling, conducted the analysis, interpreted the results, and wrote the manuscript. Ms. QIN Lufang contributed to some data for the analysis of OTMZE cutting layers. Prof. FU Yucan contributed to the discussion and background of the study. Mr. HOU Junming contributed to some experiments. All authors commented on the manuscript draft and approved the submission.

Competing interests The authors declare no competing interests.

(Production Editor: WANG Jing)

无偏置正交车铣切削层几何形状的解析模型和仿真

孙涛¹, 秦录芳¹, 傅玉灿², 侯军明³

(1. 徐州工程学院江苏省工程机械检测与控制重点实验室, 徐州 221111, 中国; 2. 南京航空航天大学机电学院, 南京 210016, 中国; 3. 南京工程学院工业中心, 南京 211167, 中国)

摘要: 正交车铣是一种高效精密的加工方法, 它的切削层直接影响切屑变形、切削力和颤振从而进一步影响刀具寿命和加工质量等。为了探究正交车铣切削层的形成过程, 研究了无偏置正交车铣切削层的几何形状。在不考虑动力学影响的情况下分析了无偏置正交车铣切削层的运动原理和形成过程, 建立了其切入/切出角、切削深度和切削厚度的解析模型。通过试验验证了该解析模型的正确性, 并分析了切削参数对铣刀切削层的影响。研究表明: 无偏置正交车铣切削层的形成可划分为两个阶段; 实际切屑形状与切削层几何形状仿真结果较为一致; 切削参数对切削层几何形状影响的程度从大到小依次为: 对应于工件每转的刀具进给量 f_a 、转速比 λ 和切削深度 a_p 。所建解析模型和研究结果为探究正偏心正交车铣切削层的形成过程提供了理论指导, 为切削层几何形状的变化提供了定量分析, 并为切削力和颤振的研究提供了理论指导。

关键词: 正交车铣; 无偏置; 切削层几何形状; 解析模型; 形成过程